Materials Today Energy 27 (2022) 101026

Contents lists available at ScienceDirect

Materials Today Energy

journal homepage: www.journals.elsevier.com/materials-today-energy/

Bifunctional catalytic activity of 2D boron monochalcogenides BX (X = S, Se, Te)

Pushkar Mishra [a], Deobrat Singh [b, *], Yogesh Sonvane [a, **], Rajeev Ahuja [b, c, ***]

[a] Applied Material Lab, Department of Physics, Sardar Vallabhbhai National Institute of Technology, Surat, 395007, India
[b] Condensed Matter Theory Group, Department of Physics and Astronomy, Box 516, Uppsala University, 75120 Uppsala, Sweden
[c] Department of Physics, Indian Institute of Technology Ropar, Rupnagar 140001, Punjab, India

ARTICLE INFO

Article history:
Received 28 September 2021
Received in revised form
22 April 2022
Accepted 23 April 2022
Available online 5 May 2022

Keywords:
Electronic properties
Charge transfer mechanism
Photocatalyst and electrocatalyst mechanism for oxygen reduction
First-principles calculations

ABSTRACT

Photocatalysis and electrocatalysis are two sustainable and renewable technologies that can meet global energy demands in environmentally friendly ways. According to recent research, 2D boron monochalcogenides in the 1 T and 2 H phases are stable, strong, and broad bandgap semiconductors. Our calculations show a strong UV absorption ability and suitable band edge positions for water splitting oxidation and reduction, making it a good choice for an efficient photocatalyst. The development of bifunctional electrocatalysts has piqued the interest of researchers working in the field of electrocatalysts for fuel cells. The electrocatalytic properties of 2D boron monochalcogenides are also investigated for catalyzing both oxygen evolution reaction (OER) and oxygen reduction reaction (ORR). The calculated overpotentials for OER/ORR mechanism are found to be 0.92/1.09 for BS (1 T), 1.00/0.59 for BS (2 H), 0.96/1.05 for BSe (1 T), 0.92/0.85 for BSe (2 H), and 1.10/0.92 for BTe (1 T), which are close to benchmark catalysts. The ORR overpotential of BS (2H) is 0.59 V, near well-known catalyst Pt (0.45 V). Therefore, our investigations indicate that the family of 2D materials, boron monochalcogenides, are promising photocatalyst and electrocatalyst candidates for OER and ORR.

1. Introduction

Photocatalysis and electrocatalysis are two critical sustainable and green approaches to satisfy the energy demands in a cleaner way effectively. At present, the difficulties in the quest for high-efficiency, low-cost, and reliable catalysts are still limited to these two technologies [1,2]. The efficiency of photocatalysts and electrocatalysts is related to the structure and design of materials. 2D materials have unique structural merits, mainly charge carrier transport, stability, active surface sites, electronic band structure, and light-absorbing properties [3]. However, 2D materials for photocatalyst present some significant challenges such as isolation, mobility of photogenerated electron-hole pairs, and light trapping at the surface of materials [4]. In order to achieve an efficient photocatalyst, the redox potential of water should lie between the conduction band edge and the valence band edge of the materials. The conduction band edge should be above H^+/H_2 redox potential, and the valence band edge should be below H_2O/O_2 oxidation potential [5,6]. In the present work, we obtained the band edge positions of all boron monochalcogenides suitable for photocatalyst, excluding the BTe (2H) phase. In the electrocatalytic procedure, the catalyst's performance is evaluated by its capability for absorption/desorption of main reaction intermediates associated with intermediate reactions. There are two basic electrochemical processes, OER and ORR, taking place in energy storage/conversion devices like metal-air batteries and renewable fuel cells. In metal-air batteries and fuel cells, i.e. galvanic mode (discharging) oxygen molecule gets reduced into water molecule and electrolytic mode (charging) water molecule gets oxidized into an oxygen molecule. However, in both reactions, redox pair O_2/H_2O is present, but the procedure of ORR is just reversed to OER [7–10].

Some other technological problems have to be resolved before their huge level applications, one of the sluggish kinetics of ORR at the time of discharging and OER during charging. For instance, the current exchange density of ORR at the cathode is much smaller

Abbreviations: OER, Oxygen Evolution Reaction; ORR, Oxygen Reduction Reaction.

* Corresponding author.
** Corresponding author.
*** Corresponding author.
E-mail addresses: deobrat.singh@physics.uu.se (D. Singh), yas@phy.svnit.ac.in (Y. Sonvane), rajeev.ahuja@physics.uu.se (R. Ahuja).

https://doi.org/10.1016/j.mtener.2022.101026

than the oxidation reaction at the anode. Additionally, OER is censorial to Zn-air batteries regarding voltage performance and recharge rate, usually lower than in the current batteries system [11]; hence, developing a bifunctional electrocatalyst for OER and ORR is remarkably advantageous in improving the recharge rate and voltage performance in rechargeable metal-air batteries. Developing a single bifunctional catalyst that is efficient for OER and ORR is, however, challenging. Platinum (Pt) and Pt-based alloys are the most effective electrocatalyst for ORR; however, they are poor electrocatalysts for OER [12–14]. On the other hand, ruthenium and iridium oxide-based electrocatalysts have excellent OER electrocatalysts, but they are poor electrocatalysts for ORR [15]. Besides this, the exorbitant prices and shortage of platinum and other valuable metals hinder the operational use of these metals as an electrolyte in energy storage/conversion devices [16]. Recently, 2D materials such as hexaaminobenzene-based coordination polymers [17], nitrogen-doped graphene [18], 2D transition-metal carbides [19], CoN_x embedded graphene [20], and transition metal-implanted 2D C_3N monolayer [21] have been widely investigated for applications in OER and ORR activity [22,23]. Becuase of a vast number of reaction sites and high activity toward OER and ORR, catalysts based on 2D materials are considered as promising candidates for OER/ORR activity. In comparison, nitrides [24] and chalcogenides [25] have also been studied for ORR. Particularly, chalcogenide materials have drawn colossal attention for OER and ORR catalyst applications because of their high electric conductivity and specific surface area (active sites) [26,27]. Ternary spinal selenide based on indium [28] and two-dimensional indium chalcogenide In_2X_3 (X = S, Se, Te) was identified as a potential photocatalyst for the overall splitting of water [29]. As far as the synthesis of materials is considered, we expect that the boron monochalcogenides monolayers can be synthesized like other group IIIA chalcogenides Ga_2S_3 [30], GaSe [31], GaTe [32], InSe [33], and In_2Te_3 [34] monolayer. The possible synthesis approaches, which can be followed are vapor phase deposition, wet chemical synthesis, and exfoliation technique.

Encouraged by the fascinating properties of chalcogenide materials toward photocatalyst for water splitting and electrocatalyst for OER and ORR activities, we have investigated the photocatalytic properties of boron monochalcogenide BX (X = S, Se, Te) for water splitting and OER/ORR activity. In this work, we have strategically investigated structural, electronic, optical, photocatalytic properties and bifunctional catalytic activity toward OER/ORR using the first-principles calculations. Our calculations demonstrated that BX (X = S, Se, Te) in both phases, 1 T and 2 H, is a bifunctional catalyst for both OER and ORR. The OER overpotential of boron monochalcogenides is even superior to valuable Pt catalyst. It is excepted that this research shed more light on 2D photocatalyst and electrocatalyst mechanism and is very useful in the design and development of highly effective multifunctional photocatalysts and electrocatalysts.

2. Computational methods

All simulations are based on density functional theory (DFT) [35]. For DFT calculations, we used the Vienna *ab-initio* simulation package (VASP) [36]. For describing core electrons, we used projector augmented wave potentials (PAW) [37]. The exchange-correlation functional has been categorized by the generalized gradient approximation (GGA) with the Perdew–Burke–Ernzerhof (PBE) functional [38]. We have used Grimme's suggested DFT-D3 to define weak Vander Waals (vdW) interactions [39]. The plane wave energy cutoff was taken as 500 eV. The k-points sampling $19 \times 19 \times 1$ is used in the Brillion zone for conjugate gradient (CG) calculation as according to Monkhorst–Pack scheme [40]. To prevent interference with the nearby layer, a vacuum of 15 Å in z-direction was used for the calculations. The convergence criterion for energy is set as 10^{-5} eV in every self-consistent loop. We relaxed the structure until the Hellmann–Feynman force on each atom had not reached equal or was less than 0.005 eV/Å.

In an acid environment, the overall OER can be defined as,

$$2H_2O \rightarrow O_2 + 4H^+ + 4e^- \quad (1)$$

The elementary reaction steps in $4e^-$ pathway are given below:

$$H_2O\ (l) + * \rightarrow *OH + e^- + H^+ \quad (a)$$

$$*OH \rightarrow *O + e^- + H^+ \quad (b)$$

$$H_2O\ (l) + *O \rightarrow *OOH + e^- + H^+ \quad (c)$$

$$*OOH \rightarrow O_2(g) + e^- + H^+ \quad (d)$$

Where * indicates a site for catalyst activity while (l) and (g) relate to the phase of the liquid and gas.

The ORR takes place by simple steps in the opposite direction of the OER.

$$O_2 + 4H^+ + 4e^- \rightarrow 2H_2O \quad (2)$$

The ORR process via the $4e^-$ transfer pathway in acidic solution is given below:

$$* + O_2(g) + e^- + H^+ \rightarrow *OOH \quad (a1)$$

$$*OOH + e^- + H^+ \rightarrow H_2O(l) + *O \quad (b1)$$

$$*O + e^- + H + \rightarrow *OH \quad (c1)$$

$$*OH + e^- + H^+ \rightarrow H_2O(l) + * \quad (d1)$$

The reaction Gibbs free energy ΔG for each step is defined by the following equation [41],

$$\Delta G = \Delta E + \Delta ZPE - T\Delta S + \Delta G_U + \Delta G_{pH} \quad (3)$$

The binding energy, zero-point energy change, and change in entropy of the absorbed state of the system and gas-phase state are represented by ΔE, ΔZPE, and ΔS. The ΔZPE and ΔS values are obtained from DFT calculation and standard thermodynamic data. $\Delta G_U = -eU$, where U is related to a standard electrode. ΔG_{pH} denotes Gibbs free energy associated with the concentration of H^+ ions, $\Delta G_{pH} = K_BT \times \ln 10 \times pH$. Using the technique proposed by Nørskov and co-workers [42], the Gibbs free energy of these element steps can be calculated. The reference electrode was adopted as the reversible hydrogen electrode (RHE), in which the proton-electron pair energy was set to half a hydrogen molecule: $\mu_{H^+} + \mu_{e^-} = (½)\mu H_2$, under conditions of U = 0 V and $P_{H_2} = 1$ bar.

For the four basic steps of OER, the free energy change can be calculated as. $\Delta G_a = \Delta G_{*OH}$, $\Delta G_b = \Delta G_{*O} - \Delta G_{*OH}$, $\Delta G_c = \Delta G_{*OOH} - \Delta G_{*O}$ $\Delta G_d = 4.92 - \Delta G_{*OOH}$. free energy change in ORR steps are calculated as, $\Delta G_{a'} = -\Delta G_d$, $\Delta G_{b'} = -\Delta G_c$, $\Delta G_{c'} = -\Delta G_b$, $\Delta G_{d'} = -\Delta G_a$.

Now, the overpotential (η) can be determined by using the following equations,

$$\eta_{OER} = \max\{\Delta G_a, \Delta G_b, \Delta G_c, \Delta G_d,\}/e - 1.23 \quad (4)$$

$$\eta_{ORR} = \max\{\Delta G_{a'}, \Delta G_{b'}, \Delta G_{c'}, \Delta G_{d'},\}/e + 1.23 \quad (5)$$

3. Results and discussion

3.1. Structural properties

The 2D boron monochalcogenides BX (X = S, Se, Te) have two phases 1 T and 2 H. In the 1 T phase, two graphene-like hexagonal monolayers of BX are arranged in such a way that chalcogenide atoms (S, Se, Te) are in the center of the hollow space of the hexagon and boron atoms are placed just above the boron atoms as demonstrated in Fig. 1 (a) and (c). ABBC generally represents the stacking of atoms. On the other side in the 2H phase structure, two graphene-like hexagonal monolayers of BX are arranged in such a way that chalcogenide atoms (S, Se, Te) are just above the chalcogenide atoms, and boron atoms are just above the boron atoms as illustrated in Fig. 1 (b) and (d) that stacking of atoms are generally represented by ABBA. The lattice constant of different structures of boron monochalcogenides BS (1 T), BS (2 H), BSe (1 T), BSe (2 H), BTe (1 T), and BTe (2 H) are lies between 3.04 Å to 3.59 Å. Our previous work [43] explains more detailed information about other structural parameters such as bond length, bond angle, and cohesive energy. Negative cohesive energies of all materials indicate the structural stability of all materials.

As for as dynamic stability is concerned, boron monochalcogenides' dynamic stability is investigated by calculating the spectrum of phonon. The calculated phonon dispersion curves are shown in Fig. S1 and these phonon dispersion curves are strongly consistent with previous studies [44]. Imaginary frequencies are absent in most boron monochalcogenide monolayers, except BTe (2 H). BTe (2 H) could be recognized as dynamic stable containing minimal imaginary frequencies (−0.224 THz) near to Γ, and if high K-points or bigger supercell will be employed in the computation, it can be corrected. Despite this, it was identified as dynamic and stable in the previous investigation [43].

Furthermore, we investigated thermal stability by performing *ab-initio* molecular dynamics (AIMD) calculations at 300 K and found that the remaining preserved structures were preserved after 5 ps as shown in Fig. 2. During the AIMD simulations, the motion (vibration from mean position) of the atoms increases compared to the equilibrium state; that is why energy fluctuates. In the energy vs. time graph (Fig. 2), the trough represents the equilibrium state of the structure (minimum energy); when atoms move away from the equilibrium state, crest forms. For MD calculations, we kept our systems at a constant temperature of 300 K for 5 ps. It was seen that after every equilibrium state, atoms behave in the same manner and a repeated pattern was obtained in the energy graph (Fig. 2). It was observed that there is no breaking of bonds between the atoms at 300 K. Therefore, the outcomes support the remarkable thermal stability of boron monochalcogenide (BX) monolayers. We conclude from the above descriptions that BX monolayers are dynamically and thermally stable.

3.2. Electronic properties

We have also investigated the electronic properties of boron chalcogenides BX (X = S, Se, Te) based on the partial density of states diagrams, as shown in Fig. 3. Electronic properties play a very important role in understanding photocatalyst and electrocatalyst activities of materials. From our previous work [43], we found that all boron monochalcogenides are wide-bandgap indirect semiconductors and bandgaps are 2.92 eV, 2.83 eV, 2.76 eV, 2.55 eV, 1.78 eV and 1.53 eV for BS (1 T), BS (2 H), BSe (1 T), BSe (2 H) BTe (1 T) and BTe (2 H), respectively. The wide indirect bandgap makes it less possible to recombine electron-hole pairs. From Fig. 3, in all boron monochalcogenide 2D materials in valence band, 3p states of the chalcogenide atoms S, Se, and Te are dominant over all the states of a boron atom, but at near Fermi level, 2p state of the boron atom is hybridized with 3p states of chalcogenide atoms. The high density of states near the Fermi level makes it easier to transfer electrons from the valence band near the bottom of the conduction band, 2p state of the boron atom is dominant over all the states of

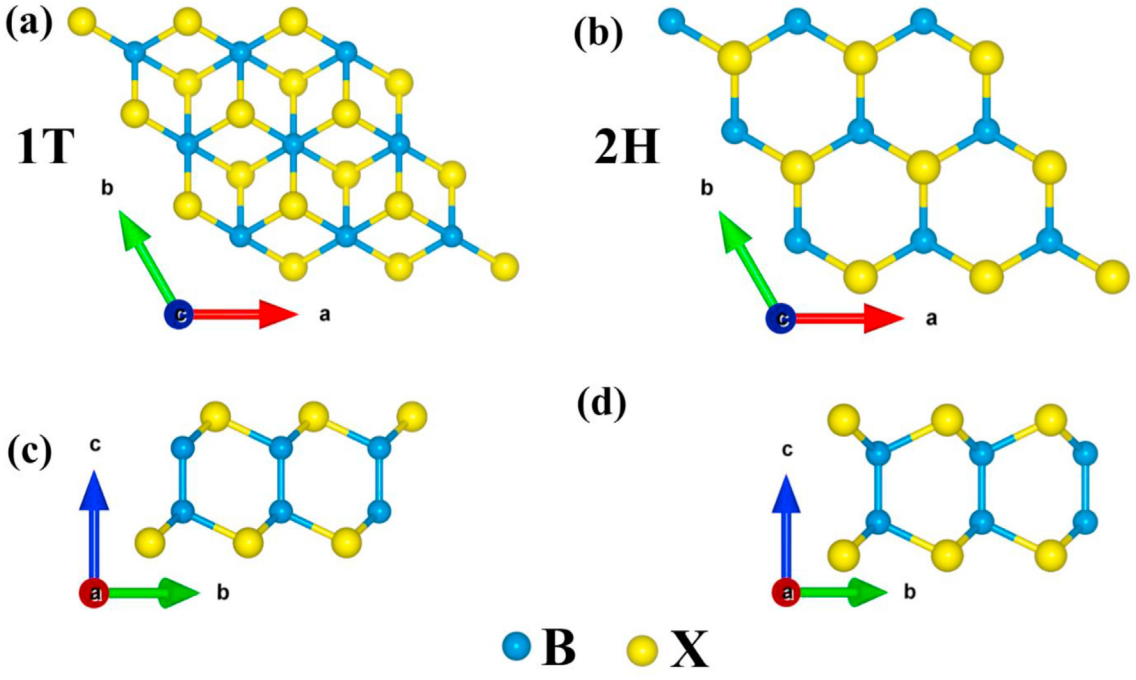

Fig. 1. Relaxed structures of boron monochalcogenides, (a) and (c) top view and side view of 1 T phase, (b) and (d) top view and side view of 2 H phase.

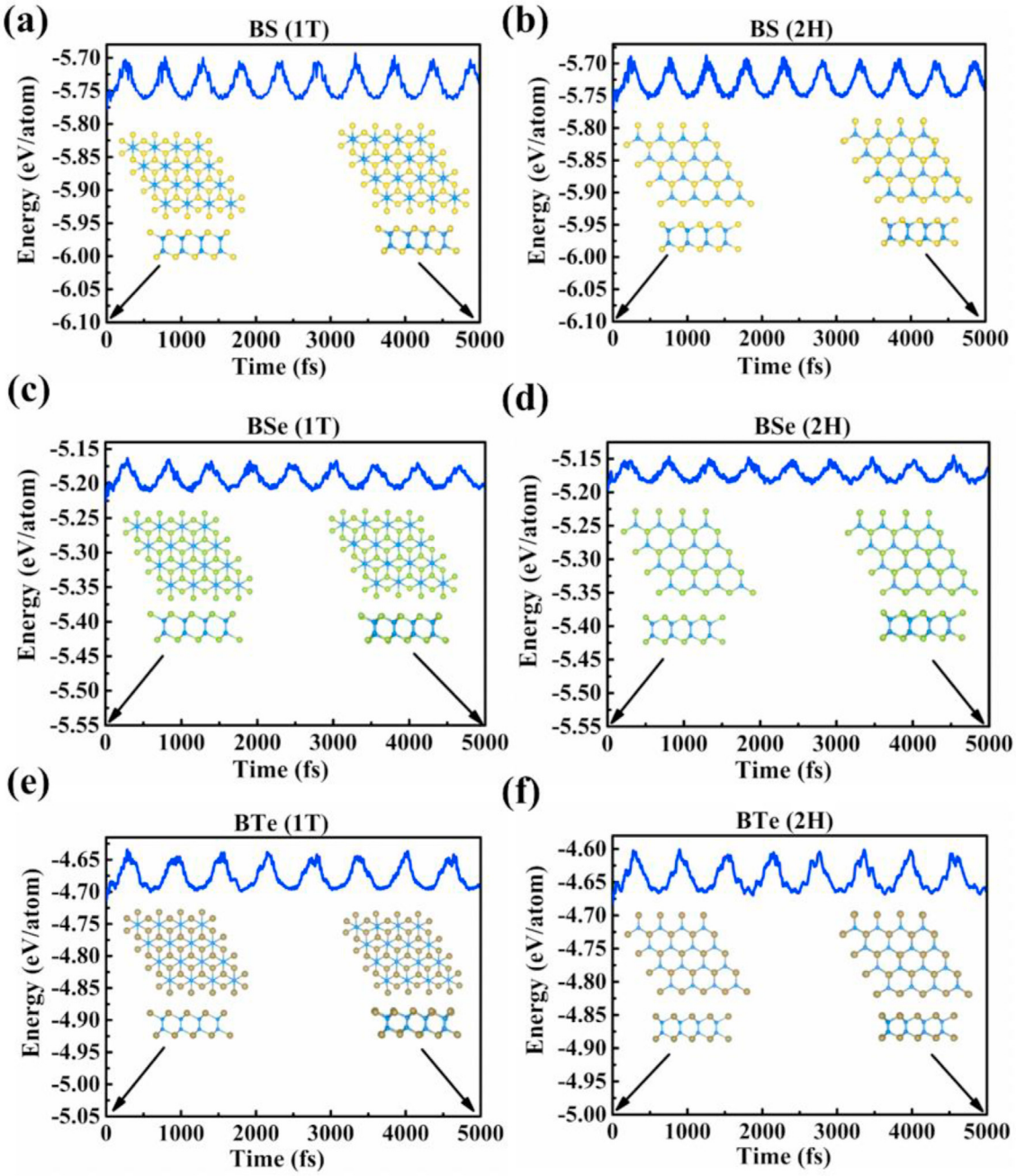

Fig. 2. AIMD simulations at 300 K for the evolution of total energy per atom in 5000 fs for (a) BS (1 T), (b) BS (2 H), (c) BSe (1 T), (d) BSe (2 H), (e) BTe (1 T), and (f) BTe (2 H) monolayers. The atomic structure at the start and end of the AIMD simulation is shown in the inset diagrams.

chalcogenide atoms (S, Se, and Te). On moving toward high energy levels, in the case of BS and BSe monolayers such as 1 T and 2 H phase, 2p state of boron atom hybridized with 3p state of S atom and in case of BSe, 2p state of B atom hybridized with 4p state of Se atom. In the case of BTe monolayers in both 1 T and 2 H phase, the 2p state of B atom hybridized with 5p state of Te atom but for particular energy such as 4.30 eV for 1 T phase and 4.20 eV for 2H phase 5p state of Te atom dominant over all the states.

3.3. Optical absorption

The optical properties of any material can be determined by using the equation given below

$$\varepsilon(\omega) = \varepsilon_1(\omega) + i\varepsilon_2(\omega) \tag{6}$$

where $\varepsilon(\omega)$ is the frequency-dependent dielectric function, $\varepsilon_1(\omega)$ is the real part of dielectric function obtained from the Kramers-Kronig transformation, and $\varepsilon_2(\omega)$ is the imaginary part of the dielectric function determined by using simulation over empty states.

The absorption coefficient $\alpha(\omega)$ is obtained from the equation:

$$\alpha(\omega) = \sqrt{2}\,\omega\sqrt{\sqrt{\varepsilon_1^2(\omega) + \varepsilon_2^2(\omega)} - \varepsilon_1(\omega)} \tag{7}$$

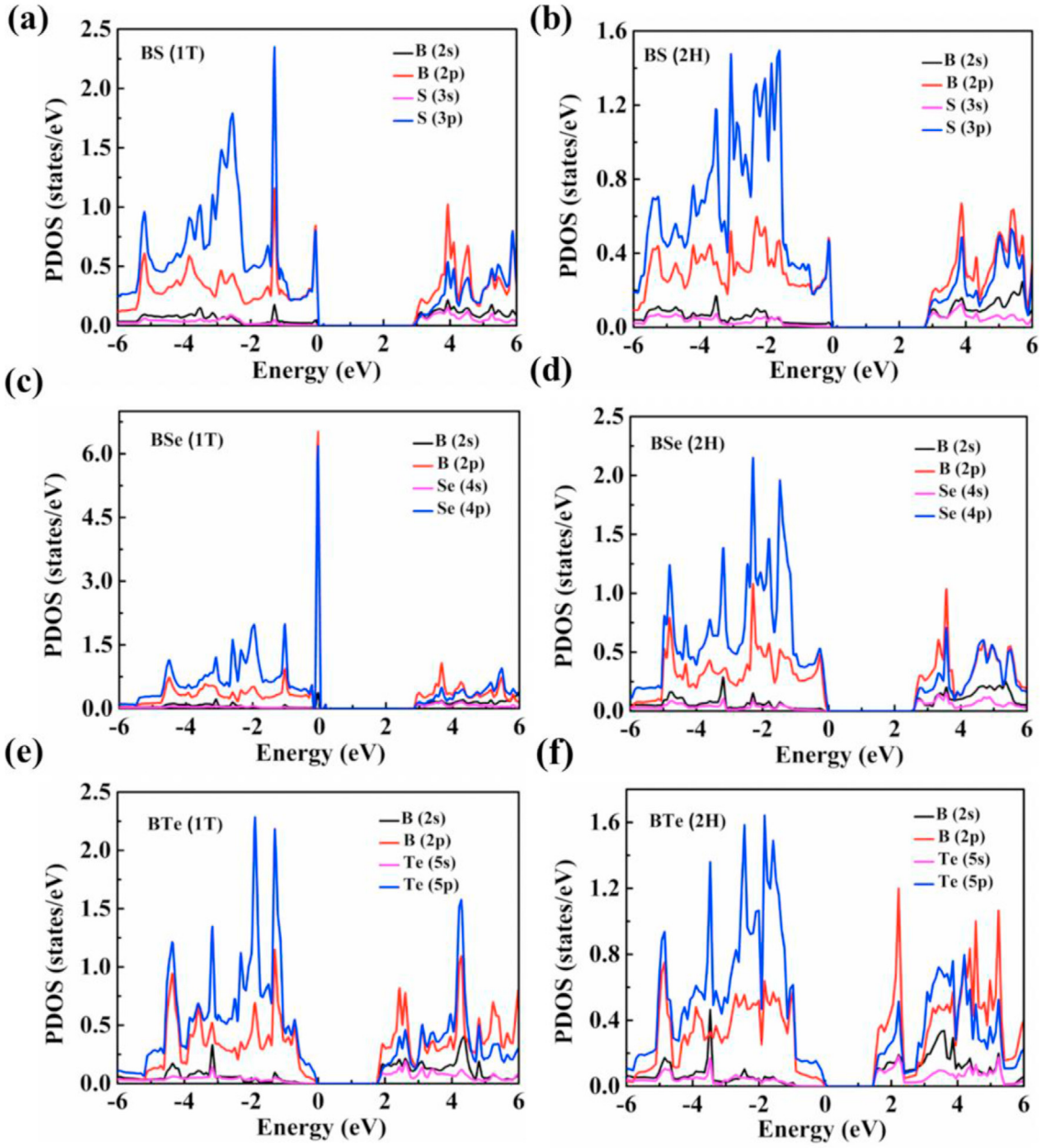

Fig. 3. PDOS of (a) BS (1 T) (b) BS (2 H) (c) BSe (1 T) (d) BSe (2 H) (e) BTe (1 T) (f) BTe (2 H) structures.

The absorption spectra of each boron monochalcogenides structure are shown in Fig. S2. We have calculated the absorption coefficient in both directions E||X (in the plane) and E||Z (out of the plane). For E||X absorption peaks occurred at 8.48 eV, 7.02 eV, 8.37 eV, 8.75 eV, 7.18 eV and 7.66 eV for BS (1 T), BS (2 H), BSe(1 T), BSe (2 H), BTe (1 T) and BTe(2 H), respectively. For E||Z absorption peaks occurred at 21.63 eV, 21.52 eV, 19.16 eV,19.45 eV, 16.88 eV, 17.11 eV for BS (1 T), BS (2 H), BSe (1 T), BSe (2 H), BTe (1 T) and BTe (2 H), respectively. According to the above data, the highest absorption peaks occur in the UV region of electromagnetic spectra. However, these are the highest absorption peaks, but there are petite curves and peaks available at a low energy level for E||Z-direction like at 6.23 eV, 6.69 eV, 6.31 eV, 6.37, eV 5.54 eV, and 8.49 eV for BS (1 T), BS (2 H), BSe (1 T), BSe (2 H), BTe (1 T), and BTe (2 H), respectively. Therefore, it is potentially advantageous in photocatalyst applications.

3.4. Photocatalytic properties

Generally, in the process of photocatalytic water-splitting, a photocatalyst (usually a semiconductor) is immersed in water. Whenever it is excited from photon energy equal to or greater than its bandgap's energy, the valence band's electrons move to the conduction band and start reducing H^+ to H_2. Although the holes stay in the valence band, the oxidation of H_2O in H^+/O_2 is started. An efficient and effective photocatalyst for water splitting must keep the conduction band edge (CB edge) above the level of water reduction (H^+/H_2) and the valence band edge (VB edge) below the

level of water oxidation (O_2/H_2O). To investigate this requirement for boron monochalcogenides, we have calculated the energy position of CB edge and VB edge by using the formulae [45]:

$$E_{CB} = \chi - E_0 - 0.5(E_g) \quad (8)$$

$$E_{VB} = E_{CB} + E_g \quad (9)$$

where E_{CB} and E_{VB} are the value of CB edge and VB edges, χ is the absolute electronegativity of BX (X = S, Se Te), Eg is bandgap energy, and E_0, the energy of free electron on hydrogen scale is 4.5 eV.

Fig. 4 shows the CB edge and VB edge of BX monolayers. As shown in Fig. 4, the BS (1 T), BS (2 H), BSe (1 T), and BSe (2 H) contain a strong capacity for reducing H^+ to H_2 because its CB edge is more negative to the water reduction potential of H^+/H_2 (0 eV vs. NHE). Other than this, the VB edge is also lower than water oxidation potential (1.23 eV vs. NHE); hence these materials also have a strong oxidizing ability to H_2O to O_2. However, in the case of BTe (1 T) and BTe (2 H), the CB edge is more negative to 0 eV, so they can easily reduce H^+ to H_2. On the other hand, the VB edge of BTe (1 T) at 1.24 eV so it can oxidize H_2O to O_2 but not as strongly as boron sulfide and boron selenide monolayers for BTe (2 H) its VB edge at 1.12 eV; unfortunately, it cannot oxidize H_2O to O_2. These results ensure that the materials BS(1 T), BS (2 H), BSe(1 T), BSe(2 H), and BTe(1 T) can split water molecules into H_2 and O_2. In addition, the absorption spectra of each boron monochalcogenides structure are shown in Fig. S2. From Fig. S2, it is evident that the highest absorption peaks exist in the ultraviolet (UV) region of electromagnetic spectra. Consequently, these materials are useful in photocatalyst applications.

3.5. Bifunctional electrocatalytic for OER/ORR activity

Now, we moved to the OER and ORR performance of boron monochalcogenides. In the OER process, there are four elementary steps. In the first step, the H_2O molecule split into H^+ and *OH on the catalyst's surface (the *OH represents that OH is adsorbed on the catalyst's surface). In the second step, *OH split into an H^+ and adsorbing *O. In step third, *O reacts with another H_2O molecule and forms *OOH. O_2 is formed and liberated from the catalyst surface in the fourth step. We have examined the most favorable site for oxygenated intermediates (*OH, *O, *OOH) for absorption on boron monochalcogenide monolayers. We found that at the near of chalcogenide atoms (S, Se, Te) are energetically favorable sites for absorption of oxygenated intermediates. Fig. 5 and Fig. 6 show the relaxed structure of BX monolayers with intermediates (*O, *OH and *OOH).

Fig. 7 illustrates the free energy diagram for BX (1 T) and BX (2 H) formation of *OH, *O, *OOH, and O_2 steps for OER and similarly reverses this for ORR. From Fig. 7(a) and (b) for BS (1 T) and BS (2 H), *OH is the potential-limiting step for OER. The overpotential for OER (η_{OER}) we got from our calculation is 0.92 V and 1.00 V. From Fig. 7(c) for BSe (1 T), *OOH is the potential-limiting step for OER, and corresponding overpotential (η_{OER}) is 0.96 V. From Fig. 7(d), *OH is the potential-limiting step in the case of BSe (2 H) and overpotential (η_{OER}) is found to be 0.92 V. From Fig. 7(e) and (f) for BTe (1 T) and BTe (2 H) for both *OOH is a potential-limiting step and the corresponding overpotential are found to be 1.10 V and 0.97 V, respectively.

Additionally, ORR is just the reverse of the OER mechanism. From the free energy diagram in Fig. 7(a), for BS (1 T) O_2 to *OOH, protonation acts as the potential-limiting step and the overpotential for ORR (η_{ORR}) is 1.09 V. In Fig. 7(b), for BS (2 H) process, *OOH to *O functions as the potential-limiting step and the overpotential (η_{ORR}) is 0.59 V, which is comparable to most commonly accepted Pt catalysts (η_{ORR} = 0.45 V) [46]. In Fig. 7(c), for BSe (1 T), protonation of O_2 to *OOH works as the potential-limiting step and the overpotential is (η_{ORR}) 1.05 V. In Fig. 7(d), for BSe (2 H) reduction, protonation of of O to *OH acts as the potential-limiting step and the overpotential (η_{ORR}) is 0.85 V. In Fig. 7(e) and (f), in the case of both BTe (1 T) and BTe (2 H), protonation of O_2 to *OOH acts as the potential-limiting step and the overpotentials (η_{ORR}) are 0.92 V and 0.73 V, respectively.

In order to describe the bifunctional electrocatalytic activity, we used the sum of OER and ORR overpotential $\eta_{OER/ORR}$ as a measure. It has been identified that boron monochalcogenides monolayers

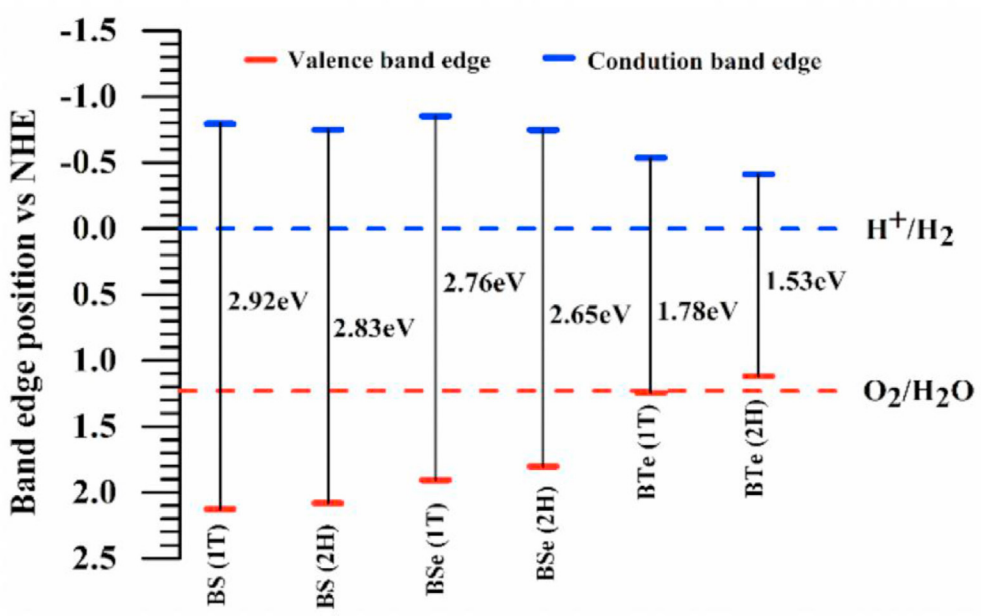

Fig. 4. The band edge positions of boron monochalcogenides with respect to water oxidation and reductions potential levels.

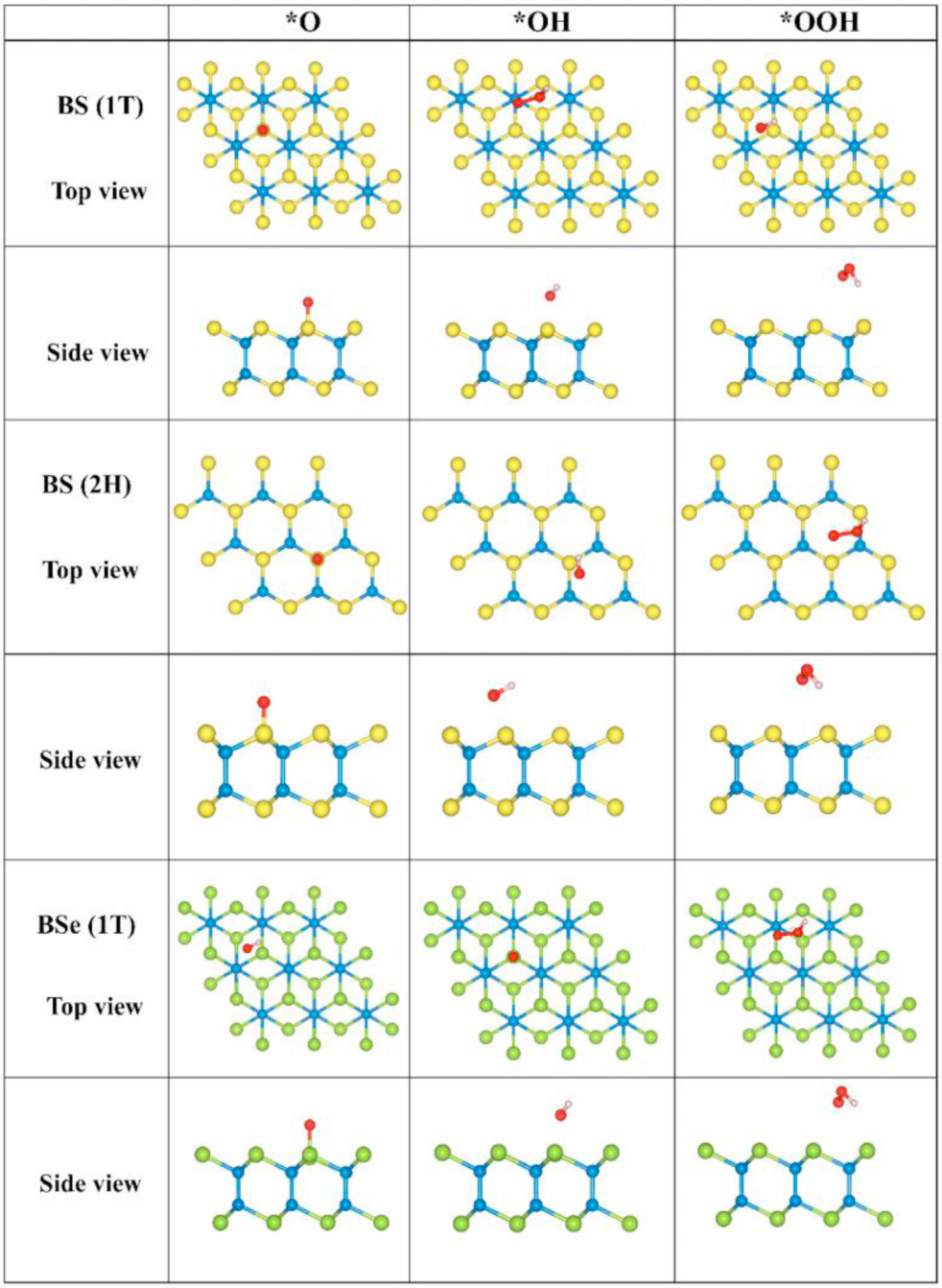

Fig. 5. The top view and side view of the relaxed structure after adsorption of *O, *OH, *OOH on BS (1 T), BS (2 H), and BSe (1 T).

are promising bifunctional electrocatalysts whose $\eta_{OER/ORR}$ are found to be 0.92/1.09: 2.01 V for BS(1 T), 1.00/0.59; 1.59 V for BS (2 H), 0.96/1.05; 2.01 V for BSe (1 T), 0.92/0.85; 1.77 V for BSe (2 H), 1.10/0.92; 2.02 V for BTe (1 T) and 0.97/0.73 1.70 V for BTe (2 H). The calculated values of $\eta_{OER/ORR}$ are comparable to Pt (1.23/0.45; 1.68 V) and IrO_2 (0.65/1.12; 1.77 V) [47], particularly with regard to all boron monochalcogenides, 2 H phase structure such as BS (2 H), and BSe (2 H) shows the superior performance bifunctional OER/ORR electrocatalytic activity. For comparison, the overpotential values for the OER/ORR mechanism of recently reported pristine 2D materials are summarized in Table 1. In Table 1, we observe that the overpotentials of boron monochalcogenides are less for some materials and a little bit high for some materials. It was seen that the η_{ORR} is higher in the present work as compared to 2D boron phosphide [48] and β-Sb monolayer [49].

3.6. Evaluation of electrocatalytic activity

All the above results suggest that boron monochalcogenide shows satisfactory performance for both OER and ORR activity. For better understating of kinetic of electrocatalytic activity, Bader charge analysis, isosurface charge density plots, and partial density of states (PDOS) with oxygenated intermediates (*O, *OH, *OOH) are analyzed comparatively for hybridization of states and charge

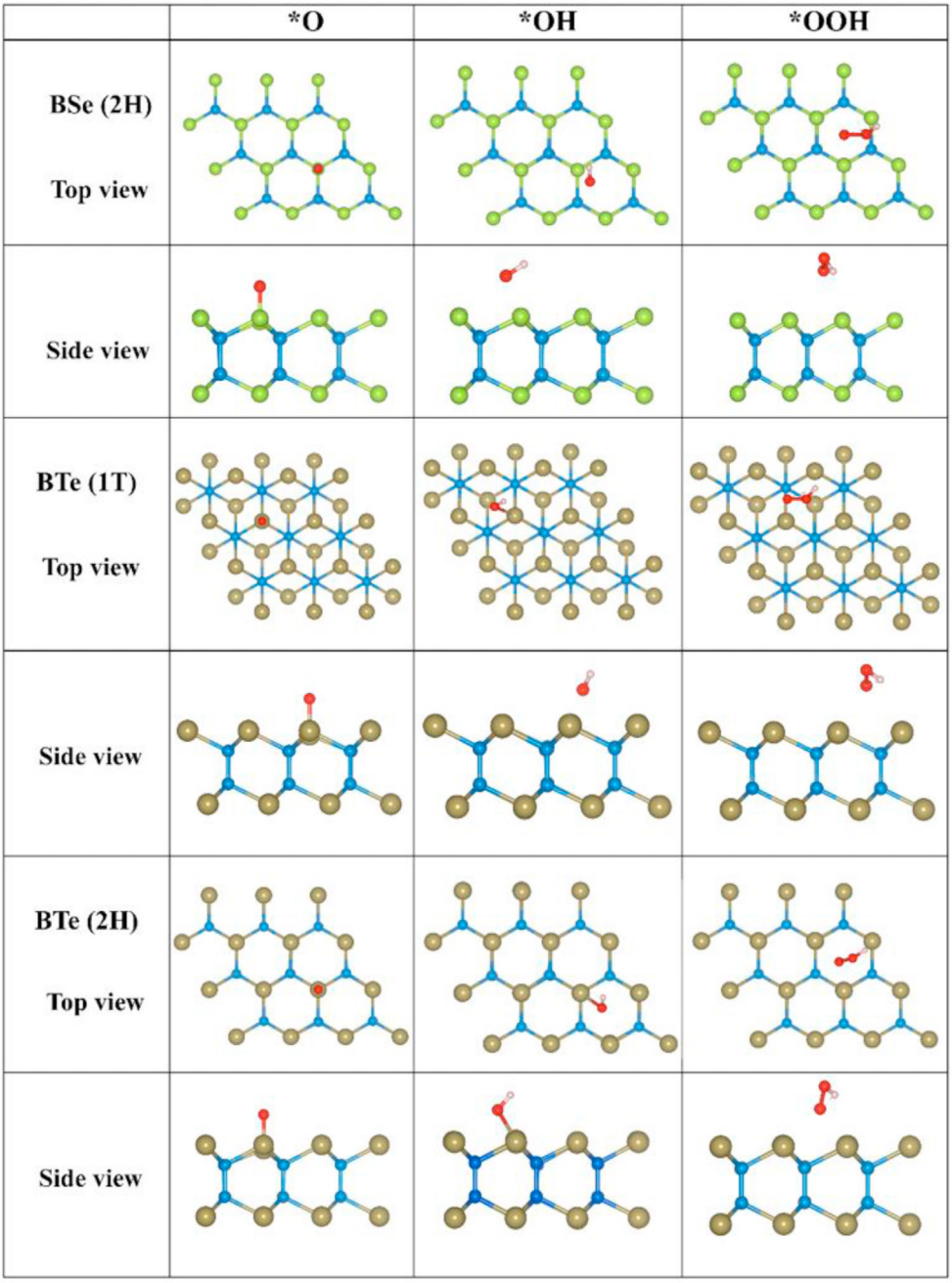

Fig. 6. The top view and side view of relaxed structure after adsorption of *O, *OH, *OOH on BSe (2 H), BTe (1 T) and BTe (2 H).

transfer analysis [13,14]. In Table 2, *O atom gets the maximum charge although moving toward heavier chalcogenide atoms it decreases, *OH obtained less charge and *OOH get the minimum charge resulting in *O strongly is interacted with chalcogenide atoms of the monolayer. Since at monolayer O, OH, and OOH are optimized at the top of chalcogenide atoms. Hence, we consider that these charges are mostly transferred from the chalcogenide's atom (S, Se, Te). For visualization of charge transfer, we have plotted the isosurface charge density profile (Fig. S3 and Fig. S4), i.e. accumulation of charge (yellow color) exists across the adsorbed *O atom and depletion of charge (cyan color) located near the chalcogenide atoms. On moving *OH and *OOH yellow area gradually decreases due to weakening attraction between chalcogenide atoms and *OH, *OOH.

These outcomes can be better described by investigating PDOS. From Fig. S5 and Fig. S6, in the case of BS (1 T) and BS (2 H) near Fermi level peak of O-p state is just below the peak of S-p states, which shows nearly all charge transfer to O atom and O atom is strongly bounded with S atom which shows the ionic character of bonding. In the case of BSe(1 T), BSe (2 H), BTe (1 T), and BTe (2 H), however, O-p states overlap with the Se-p state and Te p-states, which implies that the p state of the O atom is hybridized with the p state of Se and Te atoms. It means that it shows covalent nature of the binding, which makes it more active toward OER/ORR activity for bifunctionality.

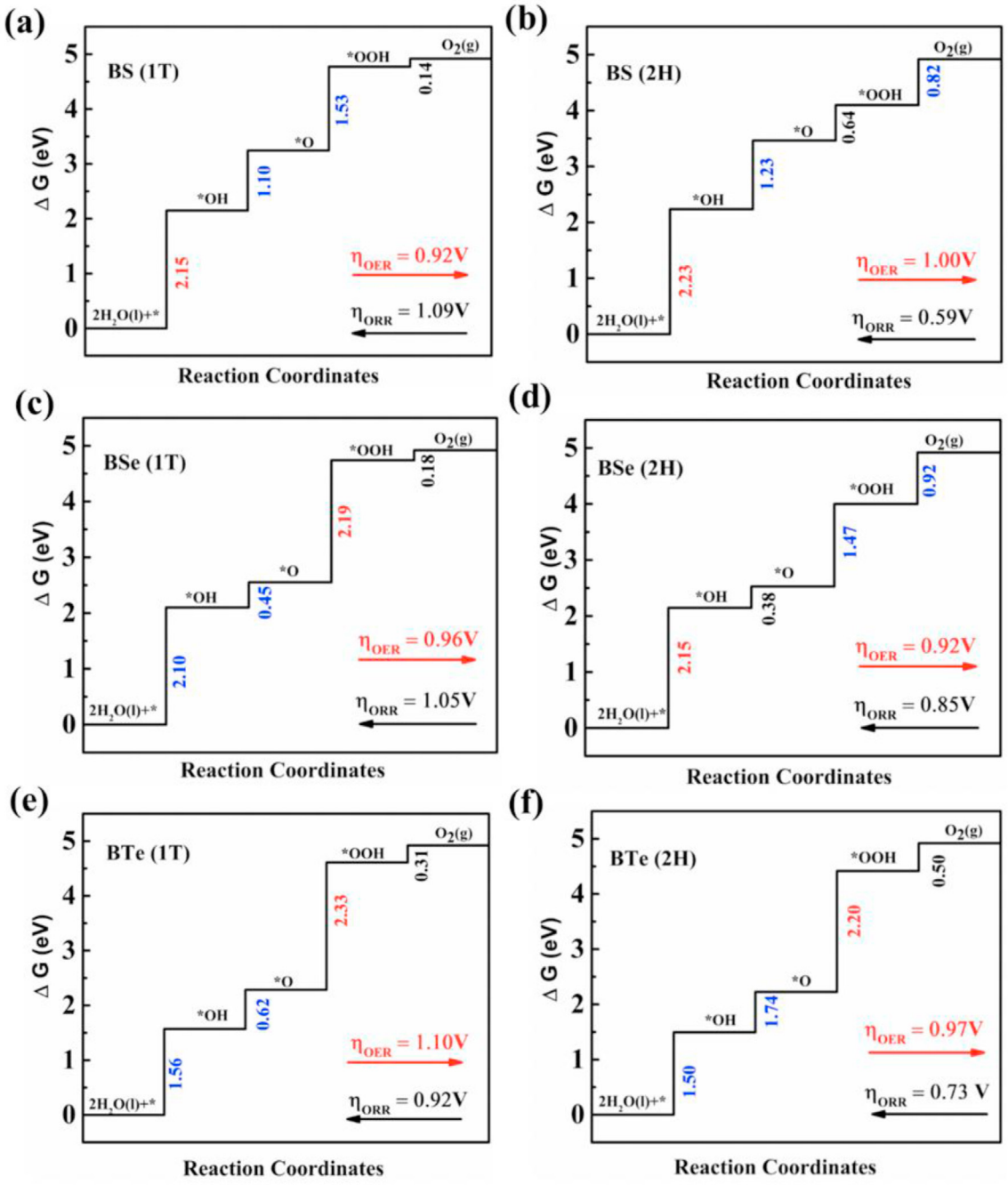

Fig. 7. Calculated free energy diagrams of OER and ORR pathways for boron monochalcogenides, where the potential limiting steps are marked in red and black colors.

Table 1
Over potentials (η_{OER} and η_{ORR}) for OER/ORR of previously reported pristine 2D materials.

Pristine 2D materials	Ref	η_{OER}	η_{ORR}
Boron Phosphide	[48]	1.62	0.67
β-Sb monolayer	[49]	0.73	0.35
Black arsenene	[50]	1.85	2.19
Mo_2B_2 monolayer	[51]	2.67	1.50
Black phosphorene	[52]	3.03	2.02
SiP homo-bilayer	[53]	1.59	1.66
SiAs homo-bilayer	[53]	2.06	1.68

Table 2
Charge transfer in the unit of e^- in case of *O, *OH, *OOH species from boron monochalcogenide monolayers.

	*O (e^-)	*OH(e^-)	*OOH(e^-)
BS (1T)	1.93436	0.38560	0.08045
BS(2H)	1.94216	0.37649	0.09026
BSe(1T)	1.79052	0.44453	0.16256
BSe(2H)	1.79393	0.43644	0.25235
BTe(1T)	1.76620	0.90131	0.30885
BTe(2H)	1.77247	0.64454	0.42763

4. Conclusions

In summary, we examined structural, electronic, photocatalytic, and electrocatalytic activity toward OER and ORR by DFT calculations. The boron monochalcogenides BX (X = S, Se, Te) monolayers are wide bandgap semiconductors. Moreover, the band edge positions of boron monochalcogenides confirm its excellent ability to trigger reduction and oxidation reactions for water splitting except for BTe (2 H). Therefore, BX monolayers can be recognized as an excellent water-splitting photocatalyst. We have also studied the activity of the BX monolayer for both OER and ORR. It is observed that the BX monolayer system demonstrates fair activity OER and ORR. The overpotentials for both OER and ORR are good enough for all monolayers. In the present work, the 2D BS (2 H)/BSe (2 H) monolayers are good candidates for OER/ORR catalyst, with the calculated overpotential η_{OER}/η_{ORR} values found to be 1.00/0.59 V and 0.92/0.85 V, respectively. The results can be potentially useful for developing photocatalyst and oxygen redox (OER/ORR) bifunctional catalysts.

Author statement

Pushkar Mishra: Investigation, Formal analysis, Methodology, Visualization, Writing - original draft. **Deobrat Singh:** Conceptualization, Formal analysis, Investigation, Methodology, Writing - review and editing, Validation. **Yogesh Sonvane:** Funding acquisition, Resources, Software, Writing - review and editing, Validation. **Rajeev Ahuja:** Funding acquisition, Project administration, Resources, Software, Supervision, Writing - review and editing, Validation.

Data availability statement

The raw/processed data required to reproduce these findings cannot be shared at this time due to legal or ethical reasons. Data are, however, available from the authors upon reasonable request.

Declaration of competing interest

The authors declare that they have no known competing financial interests or personal relationships that could have appeared to influence the work reported in this paper.

Acknowledgements

P. M. is thankful to SVNIT, Surat, for his Institute Research fellowship (FIR-DS17PH004). D. S. and R. A. thank the Swedish Research Council (VR-2016-06014 and VR-2020-04410) and J. Gust. Richert stiftelse, Sweden (2021-00665) for financial support. SNIC and HPC2N are acknowledged for providing the computing facilities. Y. S. is thankful to the Science and Engineering Research Board (SERB), India, for the financial support (grant number: EEQ/2016/000217).

Appendix A. Supplementary data

Supplementary data to this article can be found online at https://doi.org/10.1016/j.mtener.2022.101026.

References

[1] A.D. Handoko, S.N. Steinmann, Z.W. Seh, Theory-guided materials design: two-dimensional MXenes in electro- and photocatalysis, Nanoscale Horizons 4 (2019) 809–827, https://doi.org/10.1039/c9nh00100j.
[2] C. Chang, W. Chen, Y. Chen, Y. Chen, Y. Chen, F. Ding, C. Fan, H. Jin Fan, Z. Fan, C. Gong, Y. Gong, Q. He, X. Hong, S. Hu, W. Hu, W. Huang, Y. Huang, W. Ji, D. Li, L.-J. Li, Q. Li, L. Lin, C. Ling, M. Liu, N. Liu, Z. Liu, K. Ping Loh, J. Ma, F. Miao, H. Peng, M. Shao, L. Song, S. Su, S. Sun, C. Tan, Z. Tang, D. Wang, H. Wang, J. Wang, X. Wang, X. Wang, A.T.S. Wee, Z. Wei, Y. Wu, Z.-S. Wu, J. Xiong, Q. Xiong, W. Xu, P. Yin, H. Zeng, Z. Zeng, T. Zhai, H. Zhang, H. Zhang, Q. Zhang, T. Zhang, X. Zhang, L.-D. Zhao, M. Zhao, W. Zhao, Y. Zhao, K.-G. Zhou, X. Zhou, Y. Zhou, H. Zhu, H. Zhang, Z. Liu, Recent progress on two-dimensional materials, Acta Phys. Chim. Sin. 37 (2021), 2108017, https://doi.org/10.3866/pku.whxb202108017.
[3] F. Shojaei, B. Mortazavi, X. Zhuang, M. Azizi, Silicon diphosphide (SiP2) and silicon diarsenide (SiAs2): novel stable 2D semiconductors with high carrier mobilities, promising for water splitting photocatalysts, Mater. Today Energy 16 (2020) 100377, https://doi.org/10.1016/J.MTENER.2019.100377.
[4] H. Xu, S. Ci, Y. Ding, G. Wang, Z. Wen, Recent advances in precious metal-free bifunctional catalysts for electrochemical conversion systems, J. Mater. Chem. A. 7 (2019) 8006–8029, https://doi.org/10.1039/c9ta00833k.
[5] D. Singh, P.K. Panda, N. Khossossi, Y.K. Mishra, A. Ainane, R. Ahuja, Impact of edge structures on interfacial interactions and efficient visible-light photocatalytic activity of metal-semiconductor hybrid 2D materials, Catal. Sci. Technol. 10 (2020) 3279–3289, https://doi.org/10.1039/d0cy00420k.
[6] L. fei Hong, R. tang Guo, Y. Yuan, X. yin Ji, Z. sheng Li, Z. dong Lin, W. guo Pan, Recent progress of two-dimensional MXenes in photocatalytic applications: a review, Mater, Today Energy 18 (2020) 100521, https://doi.org/10.1016/J.MTENER.2020.100521.
[7] S. Agarwal, X. Yu, A. Manthiram, A pair of metal organic framework (MOF)-derived oxygen reduction reaction (ORR) and oxygen evolution reaction (OER) catalysts for zinc-air batteries, Mater. Today Energy 16 (2020) 100405, https://doi.org/10.1016/j.mtener.2020.100405.
[8] J. Wu, J. Zou, W. Zhang, J. Li, Z. Yang, K. Qu, Y. Li, W. Cai, Selectively etched graphene encapsulated CoFe catalyst for zinc-air battery application, Mater. Today Energy 17 (2020) 100438, https://doi.org/10.1016/j.mtener.2020.100438.
[9] Y. Li, Z. Yin, M. Cui, S. Chen, T. Ma, Bimetallic cobalt molybdenum carbide–cobalt composites as superior bifunctional oxygen electrocatalysts for Zn–air batteries, Mater. Today Energy 18 (2020) 100565, https://doi.org/10.1016/j.mtener.2020.100565.
[10] C. Alegre, C. Busacca, A. Di Blasi, O. Di Blasi, A.S. Aricò, V. Antonucci, V. Baglio, Toward more efficient and stable bifunctional electrocatalysts for oxygen electrodes using FeCo2O4/carbon nanofiber prepared by electrospinning, Mater. Today Energy 18 (2020) 100508, https://doi.org/10.1016/j.mtener.2020.100508.
[11] Y. Li, H. Dai, Recent advances in Zinc-air batteries, Chem. Soc. Rev. 43 (2014) 5257–5275, https://doi.org/10.1039/c4cs00015c.
[12] F.D. Kong, S. Zhang, G.P. Yin, N. Zhang, Z.B. Wang, C.Y. Du, Pt/porous-IrO2 nanocomposite as promising electrocatalyst for unitized regenerative fuel cell, Electrochem. Commun. 14 (2012) 63–66, https://doi.org/10.1016/j.elecom.2011.11.002.
[13] P. Li, J. Zhu, A.D. Handoko, R. Zhang, H. Wang, D. Legut, X. Wen, Z. Fu, Z.W. Seh, Q. Zhang, High-throughput theoretical optimization of the hydrogen evolution reaction on MXenes by transition metal modification, J. Mater. Chem. A. 6 (2018) 4271–4278, https://doi.org/10.1039/c8ta00173a.
[14] N. Abidi, K.R.G. Lim, Z.W. Seh, S.N. Steinmann, Atomistic modeling of electrocatalysis: are we there yet? Wiley Interdiscip. Rev. Comput. Mol. Sci. 11 (2021) https://doi.org/10.1002/wcms.1499.
[15] Y. Shao, S. Park, J. Xiao, J.G. Zhang, Y. Wang, J. Liu, Electrocatalysts for nonaqueous lithium-air batteries: status, challenges, and perspective, ACS Catal. 2 (2012) 844–857, https://doi.org/10.1021/cs300036v.
[16] S.Y. Huang, P. Ganesan, H.Y. Jung, B.N. Popov, Development of supported bifunctional oxygen electrocatalysts and corrosion-resistant gas diffusion layer for unitized regenerative fuel cell applications, J. Power Sources 198 (2012) 23–29, https://doi.org/10.1016/j.jpowsour.2011.09.071.
[17] G. Gao, E.R. Waclawik, A. Du, Computational screening of two-dimensional coordination polymers as efficient catalysts for oxygen evolution and reduction reaction, J. Catal. 352 (2017) 579–585, https://doi.org/10.1016/j.jcat.2017.06.032.
[18] M. Li, L. Zhang, Q. Xu, J. Niu, Z. Xia, N-doped graphene as catalysts for oxygen reduction and oxygen evolution reactions: theoretical considerations, J. Catal. 314 (2014) 66–72, https://doi.org/10.1016/j.jcat.2014.03.011.
[19] Y. Yu, J. Zhou, Z. Sun, Novel 2D transition-metal carbides: ultrahigh performance electrocatalysts for overall water splitting and oxygen reduction, Adv. Funct. Mater. 30 (2020) 2000570, https://doi.org/10.1002/adfm.202000570.
[20] X. Zhang, Z. Yang, Z. Lu, W. Wang, Bifunctional CoNx embedded graphene electrocatalysts for OER and ORR: a theoretical evaluation, Carbon N. Y. 130 (2018) 112–119, https://doi.org/10.1016/j.carbon.2017.12.121.
[21] Y. Zhou, G. Gao, J. Kang, W. Chu, L.W. Wang, Transition metal-embedded two-dimensional C3N as a highly active electrocatalyst for oxygen evolution and reduction reactions, J. Mater. Chem. A. 7 (2019) 12050–12059, https://doi.org/10.1039/c9ta01389j.
[22] A. Jain, Z. Wang, J.K. Nørskov, Stable two-dimensional materials for oxygen reduction and oxygen evolution reactions, ACS Energy Lett. 4 (2019) 1410–1411, https://doi.org/10.1021/ACSENERGYLETT.9B00876/SUPPL_FILE/NZ9B00876_SI_002.ZIP.
[23] D. Liang, H. Zhang, X. Ma, S. Liu, J. Mao, H. Fang, J. Yu, Z. Guo, T. Huang, MOFs-derived core-shell Co3Fe7@Fe2N nanopaticles supported on rGO as high-performance bifunctional electrocatalyst for oxygen reduction and oxygen evolution reactions, Mater. Today Energy 17 (2020) 100433, https://doi.org/10.1016/J.MTENER.2020.100433.

[24] X. Tian, J. Luo, H. Nan, Z. Fu, J. Zeng, S. Liao, Binary transition metal nitrides with enhanced activity and durability for the oxygen reduction reaction, J. Mater. Chem. A. 3 (2015) 16801–16809, https://doi.org/10.1039/c5ta04410c.
[25] M. Demirtas, M.J. Varjovi, M.M. Cicek, E. Durgun, Tuning structural and electronic properties of two-dimensional aluminum monochalcogenides: prediction of Janus Al2XX' (X/X′: O, S, Se, Te) monolayers, Phys. Rev. Mater. 4 (2020) 114003, https://doi.org/10.1103/PhysRevMaterials.4.114003.
[26] J. Masud, A.T. Swesi, W.P.R. Liyanage, M. Nath, Cobalt selenide nanostructures: an efficient bifunctional catalyst with high current density at low coverage, ACS Appl. Mater. Interfaces 8 (2016) 17292–17302, https://doi.org/10.1021/acsami.6b04862.
[27] D. Chen, Y. Zou, S. Wang, Surface chemical-functionalization of ultrathin two-dimensional nanomaterials for electrocatalysis, Mater, Today Energy 12 (2019) 250–268, https://doi.org/10.1016/J.MTENER.2019.01.006.
[28] J. Wang, X. Zheng, Y. Cao, L. Li, C. Zhong, Y. Deng, X. Han, W. Hu, Developing indium-based ternary spinel selenides for efficient solid flexible Zn-air batteries and water splitting, ACS Appl. Mater. Interfaces 12 (2020) 8115–8123, https://doi.org/10.1021/acsami.9b18304.
[29] P. Zhao, Y. Ma, X. Lv, M. Li, B. Huang, Y. Dai, Two-dimensional III2-VI3 materials: promising photocatalysts for overall water splitting under infrared light spectrum, Nano Energy 51 (2018) 533–538, https://doi.org/10.1016/j.nanoen.2018.07.010.
[30] X. Wang, Y. Sheng, R.J. Chang, J.K. Lee, Y. Zhou, S. Li, T. Chen, H. Huang, B.F. Porter, H. Bhaskaran, J.H. Warner, Chemical vapor deposition growth of two-dimensional monolayer gallium sulfide crystals using hydrogen reduction of Ga2S3, ACS Omega 3 (2018) 7897–7903, https://doi.org/10.1021/ACSOMEGA.8B00749/SUPPL_FILE/AO8B00749_SI_001.PDF.
[31] L. Tan, Q. Liu, Y. Ding, X. Lin, W. Hu, M.Q. Cai, H. Zhou, Effective shape-controlled synthesis of gallium selenide nanosheets by vapor phase deposition, Nano Res. 13 (2020) 557–563, https://doi.org/10.1007/s12274-020-2653-8.
[32] S. Siddique, C.C. Gowda, R. Tromer, S. Demiss, A.R.S. Gautam, O.E. Femi, P. Kumbhakar, D.S. Galvao, A. Chandra, C.S. Tiwary, Scalable synthesis of atomically thin gallium telluride nanosheets for supercapacitor applications, ACS Appl. Nano Mater. 4 (2021) 4829–4838, https://doi.org/10.1021/acsanm.1c00428.
[33] J. Zhou, J. Shi, Q. Zeng, Y. Chen, L. Niu, F. Liu, T. Yu, K. Suenaga, X. Liu, J. Lin, Z. Liu, InSe monolayer: synthesis, structure and ultra-high second-harmonic generation, 2D Mater. 5 (2018), 025019, https://doi.org/10.1088/2053-1583/aab390.
[34] S. Zhang, J. Zhang, B. Liu, X. Jia, G. Wang, H. Chang, Large area growth of few-layer In2Te3 films by chemical vapor deposition and its magnetoresistance properties, Sci. Rep. 9 (2019) 1–7, https://doi.org/10.1038/s41598-019-47520-x.
[35] K. Capelle, A bird's-eye view of density-functional theory, in: Brazilian J. Phys, Sociedade Brasileira de Fisica, 2006, pp. 1318–1341, https://doi.org/10.1590/s0103-97332006000700035.
[36] G. Kresse, J. Hafner, Ab initio molecular-dynamics simulation of the liquid-metalamorphous- semiconductor transition in germanium, Phys. Rev. B 49 (1994) 14251–14269, https://doi.org/10.1103/PhysRevB.49.14251.
[37] D. Joubert, From ultrasoft pseudopotentials to the projector augmented-wave method, Phys. Rev. B Condens. Matter 59 (1999) 1758–1775, https://doi.org/10.1103/PhysRevB.59.1758.
[38] J.P. Perdew, K. Burke, M. Ernzerhof, Generalized gradient approximation made simple, Phys. Rev. Lett. 77 (1996) 3865–3868, https://doi.org/10.1103/PhysRevLett.77.3865.
[39] S. Grimme, J. Antony, S. Ehrlich, H. Krieg, A consistent and accurate ab initio parametrization of density functional dispersion correction (DFT-D) for the 94 elements H-Pu, J. Chem. Phys. 132 (2010) 154104, https://doi.org/10.1063/1.3382344.
[40] H.J. Monkhorst, J.D. Pack, Special points for Brillouin-zone integrations, Phys. Rev. B 13 (1976) 5188–5192, https://doi.org/10.1103/PhysRevB.13.5188.
[41] H.A. Hansen, J. Rossmeisl, J.K. Nørskov, Surface Pourbaix diagrams and oxygen reduction activity of Pt, Ag and Ni(111) surfaces studied by DFT, Phys. Chem. Chem. Phys. 10 (2008) 3722–3730, https://doi.org/10.1039/b803956a.
[42] J. Rossmeisl, Z.W. Qu, H. Zhu, G.J. Kroes, J.K. Nørskov, Electrolysis of water on oxide surfaces, J. Electroanal. Chem. 607 (2007) 83–89, https://doi.org/10.1016/j.jelechem.2006.11.008.
[43] P. Mishra, D. Singh, Y. Sonvane, R. Ahuja, Two-dimensional boron monochalcogenide monolayer for thermoelectric material, Sustain. Energy Fuels 4 (2020) 2363–2369, https://doi.org/10.1039/d0se00004c.
[44] B. Mortazavi, T. Rabczuk, Boron monochalcogenides; stable and strong two-dimensional wide band-gap semiconductors, Energies 11 (2018) 1573, https://doi.org/10.3390/en11061573.
[45] C. Zhang, N. Jiang, S. Xu, Z. Li, X. Liu, T. Cheng, A. Han, H. Lv, W. Sun, Y. Hou, Towards high visible light photocatalytic activity in rare earth and N co-doped SrTiO3: a first principles evaluation and prediction, RSC Adv. 7 (2017) 16282–16289, https://doi.org/10.1039/c6ra27840j.
[46] J.K. Nørskov, J. Rossmeisl, A. Logadottir, L. Lindqvist, J.R. Kitchin, T. Bligaard, H. Jónsson, Origin of the overpotential for oxygen reduction at a fuel-cell cathode, J. Phys. Chem. B 108 (2004) 17886–17892, https://doi.org/10.1021/jp047349j.
[47] J. Wang, Y. Fan, S. Qi, W. Li, M. Zhao, Bifunctional HER/OER or OER/ORR catalytic activity of two-dimensional TM3(HITP)2 with TM = Fe-Zn, J. Phys. Chem. C 124 (2020) 9350–9359, https://doi.org/10.1021/acs.jpcc.0c01143.
[48] H. Zeng, X. Liu, F. Chen, Z. Chen, X. Fan, W. Lau, Single atoms on a nitrogen-doped boron phosphide monolayer: a new promising bifunctional electrocatalyst for ORR and OER, ACS Appl. Mater. Interfaces 12 (2020) 52549–52559, https://doi.org/10.1021/acsami.0c13597.
[49] D. Singh, R. Ahuja, Theoretical prediction of a Bi-doped β-antimonene monolayer as a highly efficient photocatalyst for oxygen reduction and overall water splitting, ACS Appl. Mater. Interfaces 13 (2021) 56254–56264, https://doi.org/10.1021/acsami.1c18191.
[50] S. Santisouk, P. Sengdala, X. Jiang, X.X. Xue, K.Q. Chen, Y. Feng, Tuning the electrocatalytic properties of black and gray arsenene by introducing heteroatoms, ACS Omega 6 (2021) 13124–13133, https://doi.org/10.1021/acsomega.1c00908.
[51] T. Zhang, B. Zhang, Q. Peng, J. Zhou, Z. Sun, Mo2B2MBene-supported single-atom catalysts as bifunctional HER/OER and OER/ORR electrocatalysts, J. Mater. Chem. 9 (2021) 433–441, https://doi.org/10.1039/d0ta08630d.
[52] X.X. Xue, S. Shen, X. Jiang, P. Sengdala, K. Chen, Y. Feng, Tuning the catalytic property of phosphorene for oxygen evolution and reduction reactions by changing oxidation degree, J. Phys. Chem. Lett. 10 (2019) 3440–3446, https://doi.org/10.1021/acs.jpclett.9b00891.
[53] R.N. Somaiya, D. Singh, Y. Sonvane, S.K. Gupta, R. Ahuja, Potential SiX (X = N, P, As, Sb, Bi) homo-bilayers for visible-light photocatalyst applications, Catal. Sci. Technol. 11 (2021) 4996–5013, https://doi.org/10.1039/d1cy00304f.

Pushkar Mishra is a senior project officer at IIT Madras. He was born in Kanpur, Uttar Pradesh, India. He obtained his B·Sc. and M.Sc. degree from Chhatrapati Shahu Ji Maharaj University, Kanpur. He received his PhD from the Department of physics, Sardar Vallabhbhai National Institute of Technology, Surat, under the supervision of Dr. Yogesh Sonvane. His research interests are in 2D materials for energy storage and conversions such as thermoelectric materials, materials for hydrogen storage, materials fuel cells, and materials for solar cell.

Deobrat Singh is a postdoctoral researcher at Materials Theory Group, Department of Physics and Astronomy, Uppsala University, Sweden, under the supervision of Prof. Rajeev Ahuja. He has published more than 45 scientific papers in peer-reviewed journals. His research interest spans over a broad range, wherein he employs diverse computational tools to explore various significant scientific problems related to nanomaterials, catalysis, sensors, molecular electronics, and materials for energy storage, including solar cells, perovskites, batteries, thermoelectric devices and other applications of novel two-dimensional monolayer/multilayer materials.

Yogesh Sonvane was born and brought up in Surat, Gujarat, India. He did B·Sc. (Physics) from Navyug Science College, Surat, in 2005. He had completed his M.Sc. (Physics) from the Department of Physics, V·N.S. Gujarat University, Surat, in 2007. He had completed hisPh.D. from the Department of Physics, V·N.S. Gujarat University, Surat, in 2011. Then he joined the Department of Physics, S.V. National Institute of Technology as an Assistant Professor in April 2012. He has 10 years of teaching experience and 14 years of research experience. His research area is Perovskite-based solar cells, Advanced 2D Materials, Nanofluids, Liquid Metal, and its Alloy.

Rajeev Ahuja is a professor of Material Theory at Uppsala University and one of the most highly cited researchers in Sweden. He has published 1045 scientific papers (H-Index:90, i-10-index:645 & citations: 37,700). Ahuja had been elected APS-Fellow (2019), FRSC (2021), in the Advisory Board of JMCA and awarded the Beller Lectureship for APS March Meeting-2017, USA, Wallmark prize-2011 from KVA, and Eder Lilly and Sven Thureus prize and Benzelius prize from KVS. Ahuja is an elected member of KVS and served on the board of EHPRG and the executive board of the AIRAPT. Ahuja has supervised 30 PhDs and more than 35 postdocs.